# CO$_2$ Photoreduction via Quantum Tunneling: Thin TiO$_2$-Coated GaP with Coherent Interface To Achieve Electron Tunneling

Li-Fen Li, Ye-Fei Li,*[ID] and Zhi-Pan Liu*[ID]

Collaborative Innovation Center of Chemistry for Energy Material, Key Laboratory of Computational Physical Science (Ministry of Education), Shanghai Key Laboratory of Molecular Catalysis and Innovative Materials, Department of Chemistry, Fudan University, Shanghai 200433, China

S *Supporting Information*

ABSTRACT: Photocatalysts for CO$_2$ photoreduction such as GaP often suffer from poor stability due to a high reduction environment as required for CO$_2$ reduction, e.g., −1.9 V vs SCE to reach the current density of 10 mA/cm^2 at pH = 5.8 on p-GaP (Hallman, M. *Nature* **1978**, *275*, 115). The coating with stable oxides appears to be a promising solution, but many fundamental aspects such as the epitaxial relation between materials, the coating layer thickness, and the consequent photoactivity remain unknown. Here, using a thin TiO$_2$-coated GaP as a model system, we have systematically investigated the dependence of photoactivity upon the deposition of TiO$_2$ on GaP surfaces. By combining the modified phenomenological theory of Martensitic crystallography and a stochastic surface walking global search, we resolve the atomic-level structures of the interface between GaP and TiO$_2$, a set of coherent interfaces between TiO$_2$ and GaP ((001)$_{TiO2}$//(100)$_{GaP}$, (101)$_{TiO2}$//(110)$_{GaP}$, and (112)$_{TiO2}$//(100)$_{GaP}$). Due to the negligible interface strain, the epitaxial TiO$_2$ coating layer is found to be as stable as bulk TiO$_2$ even with a thickness below 1 nm, suggesting the presence of the well-ordered interface is a critical condition for promoting electron−hole separation in photocatalysis. We demonstrate that a photoelectron generated from GaP bulk can readily tunnel through the thin TiO$_2$ layer (0.5−3 nm) without significant decay, which can decrease the CO$_2$ reduction barrier significantly by 1.02 eV as compared to that without electron tunneling; alternatively, the photoelectron may also undergo lattice hopping to the TiO$_2$ surface to promote hydrogen evolution as required in water splitting. Our results rationalize the recent finding that the high CO$_2$ reduction ability of TiO$_2$ coated GaP at a critical thickness (<10 nm). Using the theoretical framework developed here, we predict that the TiO$_2$ coating strategy could be extended naturally to a range of photoabsorbing materials, including zincblende semiconductors and organic−inorganic hybrid halide perovskites, which can achieve a coherent interface and exhibit photoactivity toward water splitting and CO$_2$ reduction.
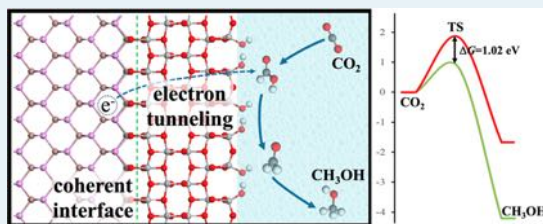
KEYWORDS: *heteromaterial, photocatalysis, CO$_2$ reduction, DFT, electron tunneling*

1. INTRODUCTION

CO$_2$ reduction under visible light is critical for CO$_2$ abatement and also for utilizing solar energy to make useful chemicals.[1,2] Due to the high overpotential as required for CO$_2$ photoreduction, common photoabsorbing materials such as TiO$_2$ and ZnO are unable to catalyze the reaction thermodynamically. On the other hand, GaP with a conduction band minimum (CBM) at −1.2 V relative to SHE (cf. TiO$_2$ −0.2 V, ZnO, −0.2 V)[3] satisfies the thermodynamic requirement for CO$_2$ reduction, but the experiments show that GaP is extremely unstable under CO$_2$ reduction conditions: this material corrodes rapidly and degrades significantly even within 30 min of illumination.[4] The coating of GaP by other stable oxides with either crystalline or amorphous form would be a natural solution.[4−12] A key challenge in this field is to search for a novel coating material that can grow into a stable thin film on the photoabsorbing materials. Indeed, Zeng et al. showed that the passivated GaP by crystalline TiO$_2$ coating with anatase form exhibits both high activity and high stability for CO$_2$ reduction.[4] The passivated GaP with thin-layer TiO$_2$

achieves the highest activity at a critical thickness of ∼10 nm.[4] To date, many fundamental aspects for these nanoscale composite materials remain largely unknown, ranging from the atomic interface structure to the photoelectron migration pathways and to the photoactivity.

Taking TiO$_2$/GaP composite material as an example, the enhanced activity on ultrathin TiO$_2$-coated GaP may be generally attributed to two possible reasons. The first is that the intrinsic catalytic activity of epitaxial TiO$_2$ on GaP is significantly different from that of bulk TiO$_2$, due to the surface strain and the interaction with GaP substrate.[13] The second is that, when the thickness of TiO$_2$ is on the nanometer scale, quantum tunneling becomes significant for electron transport.[5] In such a tunneling mechanism, the energy of tunneled electron may be much higher than CBM of TiO$_2$, which promotes CO$_2$ reduction. Regardless of the reasons, GaP/TiO$_2$ interface plays a vital role in the enhanced activity of CO$_2$

reduction. Unraveling the interface structure is, therefore, the essential step toward understanding the origin of enhanced activity for CO_2 reduction. Furthermore, most group III–V (e.g., InP, GaAs) and group IV semiconductors (e.g., C, Si, Ge) share the same zincblende structure, and the TiO_2 coating layer is the common protector layer on these materials. Understanding the interface structures between semiconductor substrate and TiO_2 coating layer shows general significance.

While theoretical simulation is a useful tool to clarify the interfacial structure, a significant problem encountered in predictions of interfacial structures is the lack of information on the lattice/surface relationship at the interface.[14] In previous theoretical studies, the heteromaterials were constructed manually by gluing two phases using their low Miller index surfaces. Such an approach has two severe problems: (i) It is virtually unlikely to numerate all possible orientation relations (OR) for the heteromaterial. In fact, most previous studies only consider one likely OR as suggested from the lattice parameter.[15] (ii) The size of the supercell is important for reducing the strain of interface, which is, however, difficult to optimize by a manual approach since the large supercell calculations are computationally expensive from first principles. Therefore, an algorithm to optimize ORs and supercell size for heterophase/material interfaces is highly desirable for identifying stable heterojunctions.

In this paper, we develop a modified phenomenological theory of Martensitic crystallography (PTMC)[16−18] to search for all possible low-strain interfaces in heteromaterial systems. The heterophase junction between GaP and anatase TiO_2 is focused, since the enhanced activity of CO_2 reduction was observed on the anatase-TiO_2-coated GaP photocathode.[4] After screening out the low-strain interfaces, we further identify the atomic structure of the interfacial structures via recently developed surface stochastic walking (SSW) global optimization.[19−22] Our results prove that the coherent interfaces for GaP/TiO_2 are present and can grow on GaP (110) and GaP (100) and stabilize TiO_2 protector layers as thin as 1 nm (<6 atomic layers thickness). By evaluating CO_2 reduction kinetics on 1 nm TiO_2 coated GaP, we show that the quantum tunneling plays an important role in enhancing the CO_2 reduction to methanol.

This paper is organized as follows. The methodology for the modified PTMC theory and DFT calculations are described in section 2. Our main results, including the atomic structures for GaP/TiO_2 junction, the quantum-tunneling efficiency of carriers through the TiO_2 coating, and the reaction kinetics for CO_2 reduction are detailed in section 3. In section 4, we discuss the origin for the critical thickness of TiO_2 coating in CO_2 reduction and tentatively apply the modified PTMC for finding stable TiO_2-coated photovoltaic materials in general. Our main conclusions are presented in section 5.

2. METHODS

2.1. Determining ORs of Low-Strain Interfaces Using Modified PTMC.
In martensitic transformation, PTMC[16−18] is a tool to explain the observed ORs of habit planes. The calculations of PTMC require lattice correspondence of two phases as input. Based on the lattice correspondence, we can build a deformation gradient. With the deformation gradient, the directions of invariant line strain are determined, which then produce the invariant plane (habit plane). The detailed description of PTMC can be found in the Supporting Information (SI) and ref 16−18.

The idea of PTMC can be further generalized to predict the ORs of low-strain interfaces in heteromaterials. In heteromaterials, the lattice correspondence between two phases is no longer restricted by phase transition, and any lattice correspondence between two phases can be used as an input of PTMC. The definition of a unit cell is arbitrary as long as it fulfills the translational symmetry of lattice. The different definitions may result in different lattice correspondence and lead to different ORs in PTMC. Therefore, to determine the ORs for low-strain interfaces in heteromaterials, we need to sample various lattice correspondences between two phases in heteromaterials.

Mathematically, the varieties of lattice parameters are represented by the lattice parameter of a primitive cell ($\mathbf{T}'$ and $\mathbf{M}'$) multiplied by transformation matrices $\mathbf{A}$ and $\mathbf{B}$, respectively

$$\mathbf{T} = \mathbf{AT}' \text{ and } \mathbf{M} = \mathbf{BM}' \tag{1}$$

where all $\mathbf{A}$, $\mathbf{B}$, $\mathbf{T}'$, $\mathbf{M}'$, $\mathbf{T}$, and $\mathbf{M}$ are 3×3 matrices. All of the elements in matrices $\mathbf{A}$ and $\mathbf{B}$ are integers. To sample the lattice correspondence, we let the elements of matrices $\mathbf{A}$ and $\mathbf{B}$ vary within the integers of $\{-2, -1, 0, 1, 2\}$. Using the lattice correspondence $\mathbf{T}$ and $\mathbf{M}$ as inputs, we can calculate the ORs of low-strain interfaces between two phases. The validity of this idea has been verified in our previous case study of CoS_2/CoOOH heterojunction.[23,24]

With the calculated ORs, we construct the atomic model for heterojunction. Then we perform a global structural search with the SSW[25] method to determine the most stable structures for the GaP/TiO_2 interface. The flowchart of the procedure is shown in Figure 1, and the detailed implementation of modified PTMC and SSW is described in the Supporting Information.

2.2. Calculation Details.
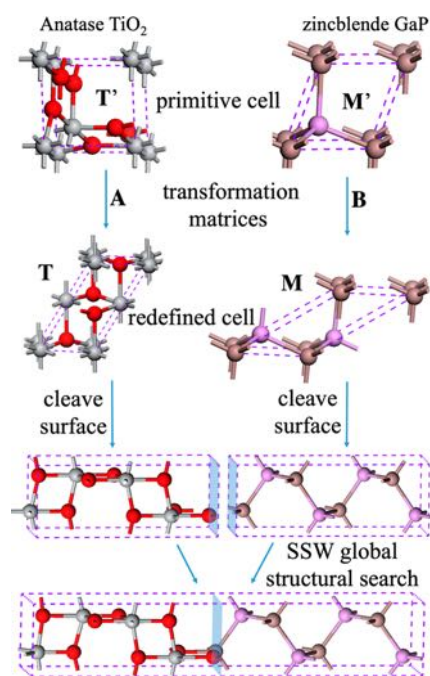All calculations in this work are based on density functional theory (DFT). The calculations for

Figure 1. Flowchart of modified PTMC utilized to determine the interfacial structure of a TiO_2/GaP heteromaterial. Key: gray balls, Ti; red balls, O; brown balls, Ga; purple balls, P.
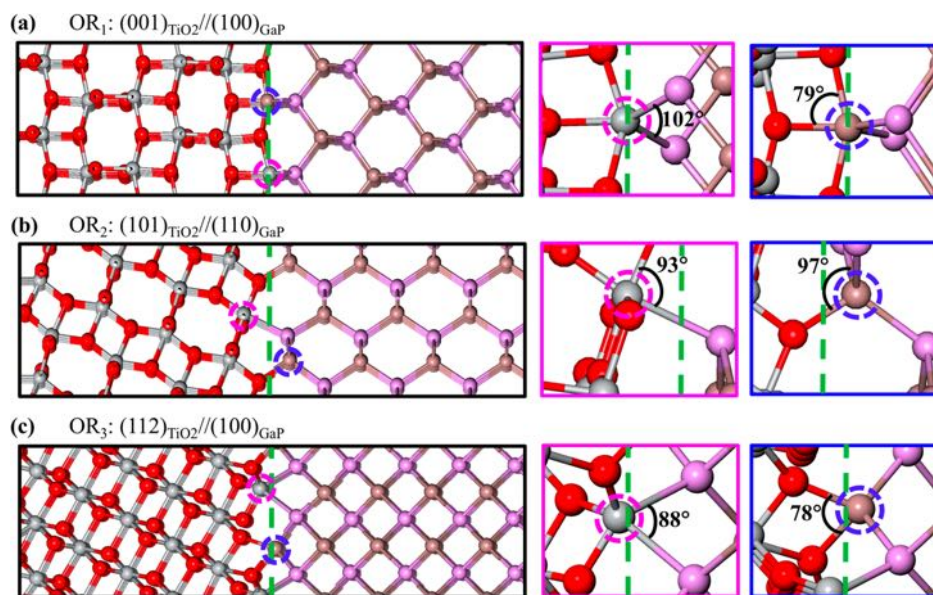
Figure 2. Atomic structures for three GaP/TiO$_2$ heterojunctions that can achieve the coherent interface. The left column is the overview of the heterojunctions. The middle and right columns are the enlarged local view of interfacial Ti and Ga ions. The green dashed lines represent the interfacial planes. The purple and blue dashed cycles highlight the interfacial Ti and Ga ions. Key: gray balls, Ti; red balls, O; brown balls, Ga; purple balls, P.

bulk geometry relaxation and interfacial energies of GaP/TiO$_2$ heteromaterials were carried out within the periodic plane wave framework as implemented in the Vienna ab initio simulation package (VASP).[26] The electron–ion interaction was represented by the projector augmented wave (PAW) type pseudopotential, and the kinetic energy cutoff of plane wave was set as 500 eV. The calculations for mechanism and kinetics for CO$_2$ reduction were performed using numerical atomic orbital basis sets and Troullier–Martins norm-conserving pseudopotentials as implemented in the SIESTA package.[27]

The exchange-correlation functional with both GGA-PBE and hybrid HSE06 have been utlized.[28,29] It should be emphasized that the hybrid HSE06 functional is believed to provide more reliable band structure and optical absorption. Our results (section 3.2) show that while the exact band level varies from PBE to HSE06, the relative band alignment is consistent in both functionals, and thus, the results from both functionals yield essentially the same conclusion (see Figure S7 for details).

The geometry convergence criterion including the transition state (TS) location as implemented in LASP code[30] was set as 0.08 e V/Å for the maximal component of force and 0.01 GPa for stress. The k-point mesh utilized was up to $(2 \times 4 \times 1)$ in the Monkhorst–Pack scheme, which was verified to be accurate enough for these bulk systems. The interfacial energies (γ) are calculated by the following equation

$$\gamma = (E_{gap/TiO2} - E_{TiO2} - E_{gap})/2A \qquad (2)$$

where $E_{GaP/TiO2}$, E_{TiO2}, and E_{GaP} are total energies for GaP/TiO$_2$ heteromaterial, TiO$_2$, and GaP, respectively. The denominator A is the interfacial area in a heterojunction.

The transmission coefficients are calculated by the transfer-matrix method.[31,32] The effective masses for electron (m_e*) and hole (m_h*) in bulk GaP and TiO$_2$ phases are chosen from the literature[33,34]

$$GaP: \; m_e* = 0.15m_e; \qquad m_h* = 0.15m_e \qquad (3)$$

$$TiO_2: \; m_e* = 0.14m_e; \qquad m_h* = 0.20m_e \qquad (4)$$

and the effective mass at the interface is averaged from those for TiO$_2$ and GaP bulks as suggested by Yao et al.[32]

2.3. Simulation Models. In this work, we utilized the supercell method (i.e., bulklike model in which TiO$_2$ and GaP layers stack together alternately) to investigate the interfacial structures and properties of GaP/TiO$_2$ heterojunctions. This approach is a common strategy for investigating the solid–solid interfaces.[14,35] In studying the electronic structure of the coating layer (for carrier transport) and the surface reactions (sections 3.2–3.4), we used a slab model consisting of a symmetrical TiO$_2$/GaP/TiO$_2$-sandwiched structure exposed to the anatase (001) surface. The most stable configuration for anatase TiO$_2$ (001) in aqueous solution is utilized as the starting structure for reaction, which is covered by 1/2 ML dissociated H$_2$O according to our previous results.[36] In this structure, half of the bridging (O$_{br}$) on the (001) surface reacts with coming H$_2$O to form two OH groups that attach to two neighboring Ti cations.

In photocatalysis, the tunneled electron should be quickly captured by a proton in solution, which leads to the formation of H on the surface.[37] From energetics, one tunneled photoelectron plus one proton in solution (pH = 0) is about 0.7 eV less stable than an adsorbed H on the surface. Furthermore, the increase of the *H coverage will lower the band position of the CBM and thus change the electrochemical potential (i.e., the Fermi level) of the material, which leads to a more negative electrochemical potential. It is therefore possible to model the concentration of the photoinduced electron via the concentration of the adsorbed H. To simulate CO$_2$ reduction under different electrochemical potentials, we considered different surface H coverages in the GaP/TiO$_2$ heterojunction system, namely 1/8, 3/8, and 1/2 monolayer (ML), where 1 ML refers to the situation where each surface lattice O atom is terminated by a H atom. From the energetics, we determine the surface-phase diagram at different electro-

chemical potentials (we set pH = 0 since CO_2 reduction on TiO_2 prefers the acidic condition[38]), as shown in Figure S11.

At −0.2 V vs SHE, i.e., being identical to the CBM level of anatase TiO_2, we found the most stable surface phase is the 1/8 ML *H covered surface. Therefore, we use the 1/8 ML *H as the initial state for CO_2 reduction without the tunneled electrons. On the other hand, we found that when the coverage of *H reaches 3/8 ML, the electrochemical potential of heteromaterial increases to −1.2 V vs SHE, being identical to the CBM position in the GaP phase.[3] Therefore, we estimate the influence of electron tunneling by calculating the energetic profiles of CO_2 reduction on the 3/8 ML *H-covered surface.

3. RESULTS

3.1. Interfacial Structures for GaP/TiO_2 Heteromaterials. Using the modified PTMC theory, we first screened out seven possible ORs with strain less than 10% (see Table S1). After SSW global optimization was performed for these seven interfaces, we finally identified three GaP/TiO_2 heteromaterials that have a coherent interface, i.e., $(001)_{TiO2}//(100)_{GaP}$, $(101)_{TiO2}//(110)_{GaP}$, and $(112)_{TiO2}//(100)_{GaP}$. It should be noted that although the strain of the second heterojunction has a relatively large strain of 7%, the interfacial energy of this heterojunction is low, that is, $0.76J/m^2$, close to the first heterojunction (0.73 J/m^2) with 2% strain. This is because a good atomic match is present for the second junction. For completeness in demonstrating our modified PTMC method to search for stable interfaces, we thus list this model as a possible interfacial structure for the GaP/TiO_2 coherent interface.

The atomic structures of the coherent interfaces are shown in Figure 2. All of the other ORs cannot form coherent interfaces as reflected from their much higher interfacial energies (>1.3 J/m^2). Considering the distinct crystal structures between GaP and TiO_2 (e.g., coordinated number and bond lengths), the presence of multiple coherent interfaces is, in fact, quite unexpected, and thus, we have analyzed their atomic structures in detail.

The most stable interface shown in Figure 2a follows the OR of $(001)_{TiO2}//(100)_{GaP}$; $[010]_{TiO2}//[110]_{GaP}$ (denoted as OR_1), with interfacial energy of 0.73 J/m^2. The lattice parameters for TiO_2 (001) and GaP (100) are 3.78 × 3.78 and 3.86 × 3.86 Å, leading to a strain of 2%. To see more clearly the atomic arrangement at the interface, we also highlight the local bonding environment for the interfacial Ti and Ga ions (Figure 2a right columns). The enlarged local view shows that apart from the pristine Ti−O and Ga−P bonds, new Ti−P and Ga−O bonds are formed in the interface. Each interfacial Ti ion bonds with two P ions of the GaP phase, while each interfacial Ga ion bonds with three O ions of the TiO_2 phase (see the middle and right columns of Figure 2a). As a result, the coordination number (CN) of the interfacial Ti and Ga ions are five, different from those in their bulk, six for Ti in bulk TiO_2, and four for Ga in bulk GaP. The structural parameters of selected Ti−P and Ga−O bonds are listed in Table 1. From Table 1, we found that the structural parameters of interfacial Ti and Ga ions are comparable. For instance, the bond length of Ti−P ($d_{Ti−P}$) and the angle of P−Ti−P ($\angle$P−Ti−P) are 2.45 Å and 102°, close to $d_{Ga−P}$ (2.43 Å) and $\angle$P−Ga−P (109°) in bulk GaP. Meanwhile, $d_{Ga−O}$ and $\angle$O−Ga−O are 2.03 Å and 79°, also close to $d_{Ti−O}$ (1.95 Å) and $\angle$O−Ti−O (77°) in bulk TiO_2. Therefore, the interfacial

Table 1. Structural Parameters of Ti−P and Ga−O Bonds in Three Coherent Interfaces

str	$OR_1{}^a$	OR_2	OR_3
γ(J/m^2)	0.73	0.76	0.83
strain (%)	2	7	2
CN_{Ti}	5(6)^b	6	5
CN_{Ga}	5(4)	4	4
$d_{Ti–P}$ (Å)	2.45(2.43)	2.68	2.62
$d_{Ga–O}$ (Å)	2.03(1.95)	2.01	1.94
$\angle$P−Ti−P (deg)	102(109)	93^c	88
$\angle$O−Ga−O (deg)	79(77)	97	78

$^a OR_1$: $(001)_{TiO2}//(100)_{GaP}$; $[010]_{TiO2}//[110]_{GaP}$. OR_2: $(101)_{TiO2}//(1\bar{1}0)_{GaP}$; $[0\bar{1}0]_{TiO2}//[110]_{GaP}$. OR_3: $(112)_{TiO2}//(100)_{GaP}$; $[\bar{2}25]_{TiO2}//[0\bar{1}0]_{GaP}$. ^{b}Values in parentheses are the structural parameters in bulk GaP and TiO_2. ^{c}In OR_2, the angles are actually $\angle$P−Ti−O and $\angle$O−Ga−P.

Ti and Ga ions can bridge well with both TiO_2 and GaP phases, forming a coherent interface.

The second most stable interface shown in Figure 2b follows the OR of $(101)_{TiO2}//(110)_{GaP}$; $[010]_{TiO2}//[110]_{GaP}$ (denoted as OR_2), with an interfacial energy of 0.76 J/m^2. The lattice parameters of TiO_2 (101) and GaP (110) are 3.78 Å × 10.21 and 3.85 Å × 10.90 Å, leading to a strain of 7%. The local view of interfacial Ti and Ga ions shows that one Ti ion bonds with one P ion of GaP matrix, while one Ga ion bonds with one O ions of TiO_2 phase (see the middle and right columns in Figure 2b). The CNs of interfacial Ti and Ga are six and four, the same as that in bulk TiO_2 and GaP. The structural parameters in Table 1 show that the bond lengths of $d_{Ti−P}$ and $d_{Ga−O}$ are 2.68 and 2.01 Å, close to that in bulk TiO_2 and GaP. While the angles of $\angle$P−Ti−O and $\angle$O−Ga−P are 93° and 97°, slightly diverge from that of $\angle$O−Ti−O (77°) and $\angle$P−Ga−P (109°) in bulk TiO_2 and GaP.

The third interface in Figure 2c follows the OR of $(112)_{TiO2}//(100)_{GaP}$; $[\bar{2}25]_{TiO2}//[0\bar{1}0]_{GaP}$ (denoted as OR_3), with an interfacial energy of 0.83 J/m^2. The lattice parameters for TiO_2 and GaP are 5.44 × 5.34 and 5.45 × 5.45 Å, with a strain of 2%. The local view shows that each interfacial Ti ion bonds with two P ions of GaP phase, while each interfacial Ga ion bonds with two O anions of the TiO_2 phase (see the middle and right columns in Figure 2c). The CNs of Ti and Ga ions in the interface are five and four, respectively. From Table 1, we show that $d_{Ga−O}$ and $\angle$O−Ga−O are 1.94 Å and 78°, close to $d_{Ti−O}$ and $\angle$O−Ti−O in bulk TiO_2. While $\angle$P−Ti−P is 88°, smaller than $\angle$P−Ga−P (109°) in he bulk GaP phase.

With the atomic structure of heterojunctions, it is intriguing to investigate the stability of the TiO_2 coating layer on the GaP matrix. The stability for the most stable heterojunction with OR_1 $(001)_{TiO2}//(100)_{GaP}$ has been computed by optimizing a series of GaP/TiO_2 heteromaterials with different TiO_2 thicknesses, i.e., 1−4 nm. Figure 3 shows that the interfacial energy gradually decreases as the thickness of TiO_2 increases: it is 0.74 J/m^2 at 1 nm and drops to 0.42 J/m^2 at 4 nm. This phenomenon can be understood by the increasing lattice match between thin TiO_2 layers and bulk TiO_2 (also GaP) with the increase of TiO_2 layers. For instance, the lattice parameters for a 1 nm thick free-standing TiO_2 slab are 3.44 × 3.44 Å, much smaller than that in bulk TiO_2 (3.78 × 3.78 Å) and GaP (3.86 × 3.86 Å). As the TiO_2 slab becomes thicker, this difference in lattice diminishes gradually, from 3.44 × 3.44 Å in 1 nm to 3.76 × 3.73 Å in 4 nm thickness.
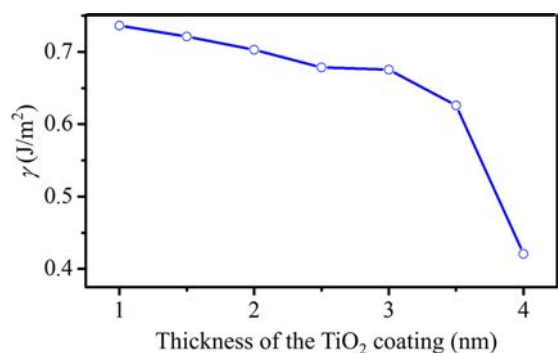
Figure 3. Interfacial energy for GaP/TiO₂ against the thickness of the TiO₂ coating.

As another proof of the stability for the interface, we have calculated the formation energies of O vacancies and compared them with those of pure anatase $TiO_2(001)$. Three different O vacancies in a 1 nm thick TiO_2 coating, i.e., the second layer (with respect to the vacuum), the third layer, and the fourth layer, are computed, which are 5.16, 4.99, and 5.30 eV, respectively. These values are very close to the energies for the

O vacancy formation in the pure anatase $TiO_2(001)$, i.e., 5.15, 5.15, and 5.45 eV at the analogous sites.

The above results indicate the stability of the TiO_2 coating layer even at 1 nm thickness is already close to that of pure TiO_2. The low interfacial energy would help to reduce the defects concentration during the film growth and thereby improve the kinetics stability of the interface. Experimentally, Chen et al. show that 2 nm TiO_2 can protect the electrode in photochemical conditions, while the electrode failed within 0.5 h in the same conditions without a TiO_2 protector layer.[5] Our theoretical results thus agree well with the experimental finding of Chen et al. We suggest that a nanometer-scale TiO_2 coating layer on GaP (110) and (100) may be enough to stabilize a photoelectrode.

3.2. Electronic Structures of GaP/TiO₂ Heteromaterial. Taking the most stable interface $(001)_{TiO2}//(100)_{GaP}$ as the example, we further investigate the electronic structures of the GaP/TiO₂ heteromaterial, which is essential to understand the carrier transport. In sections 3.2−3.4, we use the slab model consisting of a symmetrical $TiO_2/GaP/TiO_2$-sandwiched structure to study CO_2 photoreduction.

Figure 4b shows the total and projected density of states (TDOS and PDOS), where the Fermi level is defined as the
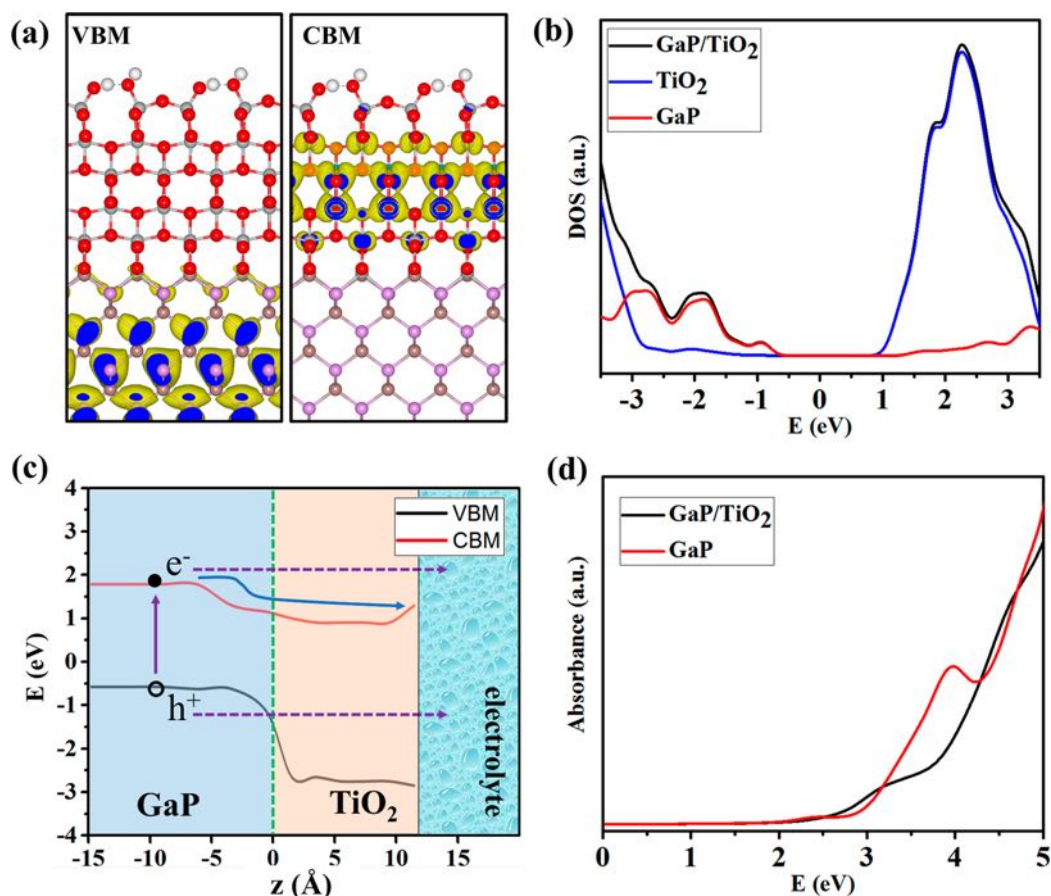

Figure 4. Electronic structures for GaP/TiO₂ heteromaterial with $(001)_{TiO2}//(100)_{GaP}$ (the PBE results are shown in Figure S7). (a) Isosurfaces of wave functions for valence band maximum (VBM) and conduction band minimum (CBM) in GaP/TiO₂ heteromaterial. The value of isosurfaces is 0.02 |e|/Å³. Key: gray balls; Ti, red balls; O, brown balls, Ga; purple balls, P. The surface of TiO₂ coating is covered by 1/2 ML dissociated H₂O in aqueous surroundings.[36] (b) Density of states (DOS) for the GaP/TiO₂ heteromaterial. The black line is the total density of states, while the blue and red lines are the projected density of states for TiO₂ and GaP compositions, respectively. The energy of E-axis is relative to the Fermi level as zero. The dotted line is the position of the Fermi level. (c) Band diagram of $(001)_{TiO2}//(100)_{GaP}$ heteromaterial. The z-axis represents the position relative to the GaP/TiO₂ interface. The red line is the band diagram of CBM, while the black line is the band diagram of VBM. (d) Optical absorption for pure GaP (red line) and GaP/TiO₂ heteromaterial (black line).

energy zero for reference. As shown from the TDOS (black line), the GaP/TiO$_2$ heteromaterial is a semiconductor with a band gap of 1.5 eV, and the states around the valence band maximum (VBM) are derived from GaP composition (red line) and not TiO$_2$ composition (blue line), as reflected by the PDOS plot. On the other hand, the states around the conduction band minimum (CBM) are derived from TiO$_2$ (blue line), well below the unoccupied states of GaP composition (red line), ∼−4.5 eV. By aligning the VBM and CBM for PDOS of each TiO$_2$ and GaP layer, we can further plot the band diagram of the heteromaterial in Figure 4c. It shows that the GaP/TiO$_2$ heteromaterial has a staggered (type II) gap, where the lowest energy state for a photoinduced hole to stay is on the GaP side while the lowest energy state for a photoinduced electron is on the TiO$_2$ side. This staggered band structure benefits the electron−hole separation at the GaP/TiO$_2$ interface in photoelectrocatalysis. We emphasize that similar conclusions can be found for the other two coherent heteromaterials with OR$_2$ and OR$_3$, as shown in Figure S3.

Besides the band diagram, the spatial distribution of wave functions is another critical issue for carrier transport through the interface. Notably, the periodic boundary condition breaks along the direction perpendicular to the interface, which usually introduces localized states in the boundary. These localized states may act as recombination centers of carriers and lower the quantum efficiency.[39] To examine the boundary states in the GaP/TiO$_2$ interface, we plotted the wave functions of VBM and CBM for GaP/TiO$_2$ heteromaterial, as shown in Figure 4a. Importantly, we found that no boundary state is present at the interface. The wave functions of VBM and CBM are delocalized in both the interface and the bulk, suggesting no energetic preference for the local trapping at the interface in the carrier transport. Similar delocalized pictures for the spatial distributions of wave functions are also found in the other two heteromaterials, OR$_2$ and OR$_3$ (see Figure S4), while the localized wave function at the VBM can be identified for the incoherent interface (see Figure S5).

It should be mentioned that the optical absorption spectrum for the coherent GaP/TiO$_2$ heteromaterial is similar to GaP bulk, suggesting that the presence of TiO$_2$ coating does not affect the photon adsorption. As shown in Figure 4d, we have compared the absorption spectra for the junction and for the pure GaP. The absorption edge of the GaP/TiO$_2$ heteromaterial is at ∼2.4 eV, being identical to that of pure GaP (∼2.4 eV), but is significantly higher than the calculated band gap (1.5 eV) of the heteromaterial. The similar onset optical absorption between the GaP/TiO$_2$ heterojunction and pure GaP indicates that the photoexcitation in the low incident photon energy largely occurs in the GaP phase. To understand the origin of the photoexcitation behavior, we have examined carefully the spatial distribution of VBM and CBM in Figure 4a, which can represent the approximate positions for electron and hole under irradiation. The results show that the VBM locates in the GaP phase, while the CBM basically locates in the TiO$_2$ phase. Therefore, a similar onset optical absorption can be attributed to the well-separated distributions of VBM and CBM (negligible wave function overlap) in the heteromaterial.

3.3. Quantum Tunneling of Carriers through the TiO$_2$ Coating. Next, we utilize the transfer-matrix method[31] to assess the quantum-tunneling efficiency for carrier through the TiO$_2$ coating. The transfer-matrix method is based on the band

theory, which assumes that the electrons travel in a static potential without dynamically interacting with lattice vibrations, other electrons, etc. This method has been widely used in the solid-state physics, and the validity of this approach has been approved in a number of material systems.[31,32] In the method, an arbitrary potential energy surface can be approximated by a stepwise potential profile characterized by sequential potential energy U_i (i is the index), where the exact solution of the Schrodinger equation is available

$$\psi_i(x) = A_i e^{ik_i x} + B_i e^{-ik_i x} \tag{5}$$

$$\psi_{i+1}(x) = A_{i+1} e^{ik_{i+1} x} + B_{i+1} e^{-ik_{i+1} x} \tag{6}$$

where $k_i = \frac{1}{\hbar}\sqrt{2m^*(E - U_i)}$ is the wave vector, m^* is the effective mass for electron or hole, $\hbar$ is the reduced Planck constant, and E is the incident energy of carrier.

Due to the continuity of $\psi_i(x)$ and $d\psi_i(x)/dx$ at each boundary, the amplitudes A_i and B_i are corrected with A_{i+1} and B_{i+1} as

$$\begin{bmatrix} A_i \\ B_i \end{bmatrix} = M_i \begin{bmatrix} A_{i+1} \\ B_{i+1} \end{bmatrix} \tag{7}$$

The transfer matrix M_i is given by

$$M_{11} = \frac{1}{2}\left(1 + \frac{m_i^*}{m_{i+1}^*}\frac{k_{i+1}}{k_i}\right)e^{-ik_i L_i}$$

$$M_{12} = \frac{1}{2}\left(1 - \frac{m_i^*}{m_{i+1}^*}\frac{k_{i+1}}{k_i}\right)e^{-ik_i L_i}$$

$$M_{21} = \frac{1}{2}\left(1 - \frac{m_i^*}{m_{i+1}^*}\frac{k_{i+1}}{k_i}\right)e^{ik_i L_i}$$

$$M_{22} = \frac{1}{2}\left(1 + \frac{m_i^*}{m_{i+1}^*}\frac{k_{i+1}}{k_i}\right)e^{ik_i L_i} \tag{8}$$

L_i is the length of one step potential. For a case of N potential steps, the total transfer matrix is calculated by multiplying transfer matrix of each step region, as

$$M = \prod_{i=1}^{i=N} M_i \tag{9}$$

The transformation coefficient T is then

$$T = \frac{m_0^*}{m_N^*}\frac{k_N}{k_0}\left(\frac{1}{M_{11}}\right)^2 \tag{10}$$

where T represents the probability of electron or hole tunneling through a potential barrier.

With the band diagram in Figure 4c, we can calculate the transmission coefficient T at different incident energies E. The incident energy equals the energy difference between photon energy and the bandgap of GaP (2.26 eV).[40] Considering the photon energy of visible light is in between 1.59 and 3.26 eV, the incident energy for carriers in the visible light region therefore varies from 0 to 1 eV. As the hole and electron tunneling are different in behavior, we discuss them separately in the following text.

Hole Tunneling. Figure 5a shows that the hole tunneling is sensitive to the thickness of TiO$_2$ coating. There is evident
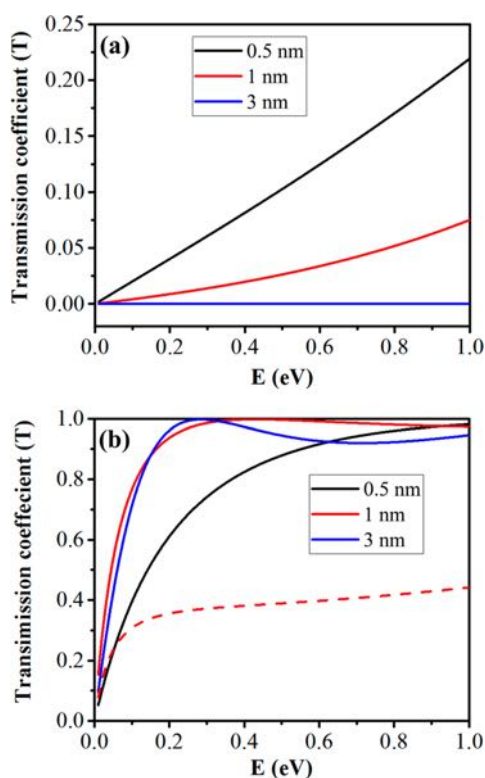
Figure 5. Plot of transmission coefficient (T) against the incident energy (E) under visible-light irradiation for the TiO_2/GaP with different TiO_2 thicknesses. (a) Hole and (b) electron tunneling through TiO_2 coating. The red dotted line in (b) is the transmission coefficient for electron tunneling through 1 nm TiO_2 coating when the interface is incoherent (see SI for details), which is much lower compared to that of the coherent interface.
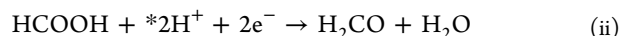
hole tunneling ($T > 0.1$) at the 0.5 nm TiO_2 coating when the incident energy >0.5 eV. The transmission coefficient decreases significantly at 1 nm TiO_2 coating, and it vanishes at 3 nm TiO_2 in the whole range of incident energy. Thus, under visible-light irradiation the hole tunneling can only occur for TiO_2 coating thinner than 3 nm. This finding is consistent with the measurement of current density on thin TiO_2 coating by Chen, Prange et al.[5] They show that when the TiO_2 thickness is below 2 nm the hole conductivity is little affected by temperature, indicating the hole transport is dominated by quantum tunneling. For a thicker (>4 nm) TiO_2 coating layer, the hole conductivity exhibits an obvious temperature dependence, indicating the hole transport proceeds via a polaron conduction mechanism.

Electron Tunneling. Figure 5b shows the transmission coefficient for electron tunneling through 0.5, 1, and 3 nm TiO_2 coating. Our results show that for all TiO_2 coating the tunneling probability is significant ($T > 0.5$ when $E > 0.2$ eV), and no appreciable decay occurs with respect to the increase of TiO_2 thickness from 0.5 to 3 nm. This indicates that the probability for electron tunneling is insensitive to the thickness of TiO_2.

It might be mentioned that the transmission coefficients for electron tunneling oscillate as the incident energy increases with the gradual narrowing for the amplitude (Figure 5b). Notably, the transmission coefficient can reach to unity in some incident energy, suggesting the completeness for electron penetration. This phenomenon is well-known as the resonance

transmission in quantum mechanics, a quantum effect when a particle transfers through a potential well.[31]

3.4. Mechanism and Kinetics for CO$_2$ reduction. Now we are the position to investigate the mechanism and kinetics for CO_2 reduction on GaP/TiO_2 heteromaterial. The reduction of CO_2 is generally believed to proceed via three proton-coupled electron transfer steps involving HCOOH, H_2CO, and CH_3OH intermediates/products.[41,42]

$$CO_2 + {}^*2H^+ + 2e^- \rightarrow HCOOH \quad\quad (i)$$

$$HCOOH + {}^*2H^+ + 2e^- \rightarrow H_2CO + H_2O \quad\quad (ii)$$

$$H_2CO + {}^*2H^+ + 2e^- \rightarrow CH_3OH \quad\quad (iii)$$

The asterisk * indicates one active site on TiO_2 surface, and e^- denotes the photoelectron in the heterojunction.

Following the three steps, we have explored the CO_2 reduction pathways on the most stable $(001)_{TiO2}//(100)_{GaP}$ heteromaterial and compared them with that on pure anatase (001). Since the electron tunneling could provide high energy electrons that promote the CO_2 reduction, we first present the reaction kinetics without the tunneled electrons and then show the enhancement of the kinetics by the tunneling.

Figure 6 shows the configurations of each key intermediate state in the CO_2 reduction over the heteromaterial. We use a 1/8 ML *H-covered surface as the initial state (i.e., adding two H atoms in each unit cell). Each H atom prefers to attach on a surface hydroxyl (i.e., forming a *OH_2, see state 1). Meantime, the electrons of H atoms would inject into the surface of heterojunction. The Fermi level of the 1/8 ML *H-covered surface is calculated to be −0.11 V related to SHE, close to the conduction band edge of anatase TiO_2 (cf. −0.2 V vs SHE), indicating these injected electrons locate on the bottom of the conduction band of TiO_2.

In the first step, CO_2 is activated by photoelectrons and a proton, i.e., following the reaction $CO_2 + {}^*H^+ + 2e^- \rightarrow HCOO^-$, which could occur via a proton-coupled electron-transfer process. *H^+ denotes one proton on a *OH_2 group. The product $HCOO^-$ then take another proton from the solution to generate HCOOH (see state 2). By a similar reaction, HCOOH is reduced to a *gem*-diol $H_2C(OH)_2$. It should be noted that, unlike other *gem*-diols, $H_2C(OH)_2$ can be stable in aqueous solutions.[43] Subsequently, $H_2C(OH)_2$ is restructured to H_2CO (see state 4) after losing H_2O. In the final step of, H_2CO is converted to CH_3OH via TS3.

The green line in Figure 6b illustrates the energetic profiles for CO_2 reduction over the heteromaterial, which shows that the barriers of $CO_2 \rightarrow HCOOH$, $HCOOH \rightarrow H_2CO$, and $H_2CO \rightarrow CH_3OH$ are 1.84, 1.82, and 1.24 eV, respectively. This result indicates that the conversions of CO_2 are very difficult, consistent with the experimentally sluggish kinetics of CO_2 reduction on GaP/TiO_2 heteromaterial under dark conditions.[44]

We noticed that compared to that on the heteromaterial, the pure anatase (001) has a higher barrier. The CO_2 reduction on this surface generally follows the same pathway as that on pure anatase (001), as shown in Figure 6a. The barriers are 1.93, 1.96, and 1.21 eV for the analogous steps. Compared with the heteromaterial, the barriers of $CO_2 \rightarrow HCOOH$ and $HCOOH \rightarrow H_2CO$ on GaP/TiO_2 heteromaterial are slightly increased by 0.1 eV, while the barrier of $H_2CO \rightarrow CH_3OH$ is same. The difference in the barriers of $CO_2 \rightarrow HCOOH$ and $HCOOH \rightarrow H_2CO$ might be attributed to the interfacial strain between
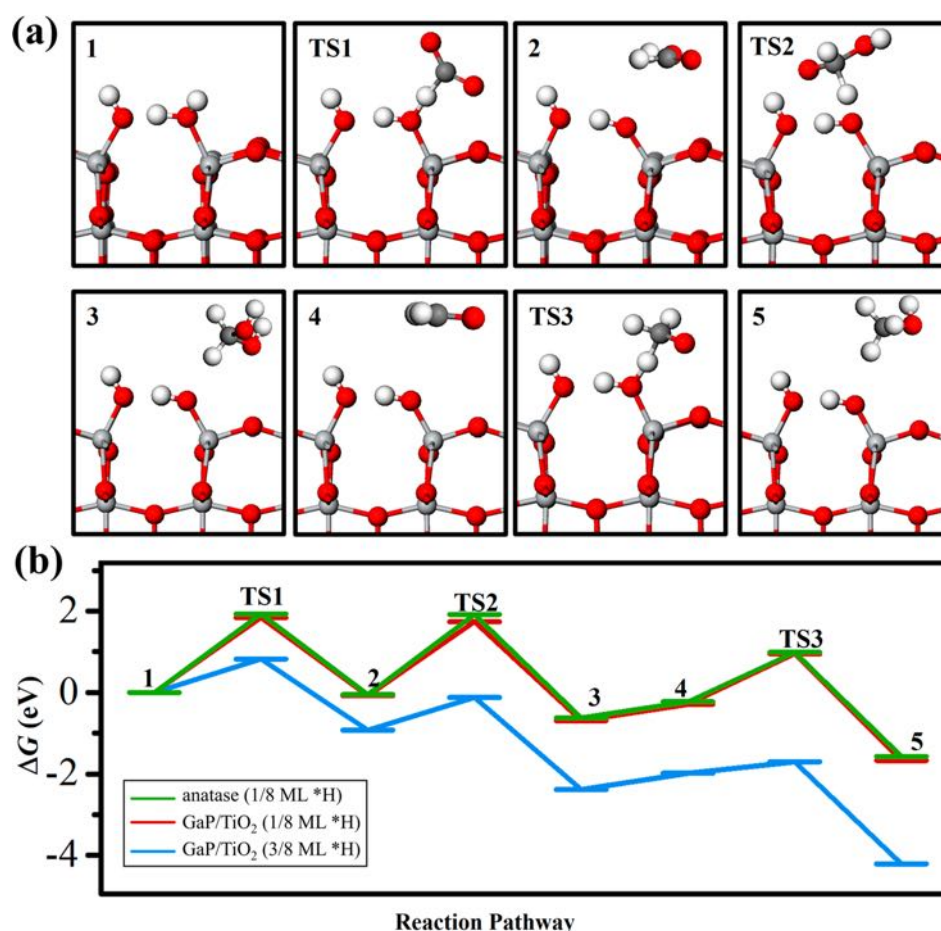
Figure 6. (a) Key intermediates of CO_2 reduction on GaP/TiO$_2$ heteromaterial with $(001)_{TiO2}//(100)_{GaP}$. Key: gray balls, Ti; red balls, O; brown balls, Ga; purple balls, P; white balls, H. (b) Energetic profiles for CO_2 reduction on the pure TiO_2 and GaP/TiO$_2$ heteromaterial. Green and red lines represent the energetic profiles without tunneling; blue line represents the energetic profiles with tunneling.

TiO_2 coating and GaP substrate. Therefore, CO_2 reduction is challenging over both catalysts.

When the electron tunneling is possible, the tunneled electrons do not lie in the CBM of TiO_2 but locate at an excited energy level in the CB of TiO_2. The high energy electron can then be quickly captured by a proton in solution forming adsorbed H on the surface. In this framework, we can approximate the effect of tunneled electrons generated by the quantum tunneling on the reaction by increasing the coverage of *H to 3/8 ML. At this higher H coverage, the electrochemical potential of heteromaterial reaches −1.2 V vs SHE, being identical to the CBM position in the GaP phase (also see section 2.3).[3] Our results show that the barriers of $CO_2 \rightarrow HCOOH$, $HCOOH \rightarrow H_2CO$, and $H_2CO \rightarrow CH_3OH$ drop to only 0.82, 0.80, and 0.28 eV, respectively (cf. 1.84, 1.82, and 1.24 eV without tunneling). This result demonstrates a significant promotion effect of quantum tunneling on the CO_2 reduction.

To elucidate the dramatic influence of quantum tunneling, we investigate the electronic structures of transition states in CO_2 reduction. Here, we use the reaction $CO_2 \rightarrow HCOOH$ as an example. In TS1, the total spin changes to 1 μ_B. Meanwhile, the spin-density isosurfaces show that the spin localizes on the CO_2 molecule as well as the adjacent *OH$_2$ group (see Figure S6). Both suggest that one electron transfers from TiO$_2$ surface to the CO_2 molecule at TS1, indicating this step is proton-coupled electron transfer (PCET), while for the reactions

$HCOOH \rightarrow H_2CO$ and $H_2CO \rightarrow CH_3OH$, the electronic structures suggest that both steps are also PCET. In a PCET event, Marcus theory has proved that the rise of energy for the transferred electron would lower the corresponding reaction barrier.[45−47] Therefore, the significant decrease of barriers with quantum tunneling can be attributed to the high energy of tunneled electron.

To summarize, our results show that the coherent interface with a thin TiO_2 coating tunnelable for electrons plays a vital role for the CO_2 reduction. With the high stability and the optical adsorption ability of the TiO$_2$/GaP system, we confirm that this material is a promising photoelectrode for CO_2 reduction.

4. DISCUSSION

4.1. Influence of TiO$_2$ Thickness on CO$_2$ Reduction. Experimentally, below a critical TiO_2 thickness (i.e., 10 nm), the activity of CO_2 reduction over heteromaterial increases progressively as the coating becomes thicker. The transmission coefficients in Figure 5b have shown that the electron tunneling is insensitive to the thickness of TiO_2 coating. The critical issue therefore lies in the stability of the as-grown TiO_2 thin film. To this point, we have shown at the end of section 3.1 that the interfacial energy gradually decreases as the TiO_2 thickness increases. The decrease of interfacial energy would refine the quality of heterogeneous interface, which benefits

the electron tunneling and thereby enhances the activity of CO_2 reduction.

On the other hand, according to Marcus theory, the rate of electron transfer is inversely related to the distance between the acceptor and donor.[45−47] Therefore, as the thickness of TiO_2 coating exceeds a critical thickness (e.g., 10 nm), the electron tunneling would become unlikely. In the thick film cases, the electron will relax to the CBM of TiO_2 and the activity of heteromaterial decays to that of pure TiO_2 phase. It should be noted that although the photoelectron that undergoes lattice hopping to the TiO_2 surface is inactive for CO_2 reduction, it should still be possible to promote hydrogen evolution required in water splitting according to the CBM level of TiO_2.

4.2. General Guideline for the Design of a Stable Photocathode of CO_2 Reduction.

Our results show that the TiO_2 coating on a semiconductor's surface may be a general strategy to develop a photocathode for CO_2 reduction as long as the following three criteria are satisfied, as schematically shown in Figure 7a. (i) The semiconductor should have
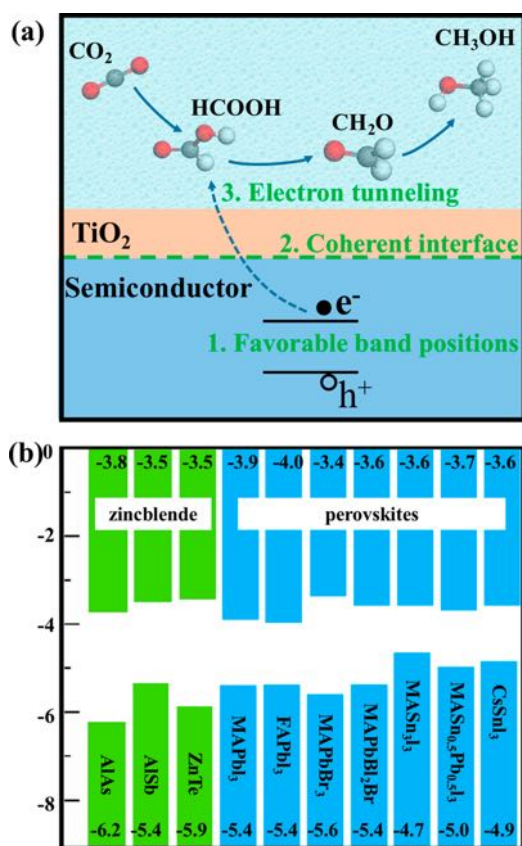

Figure 7. (a) Criteria of good photocatalysts for visible light CO_2 photoreduction. (b) Semiconductors with suitable band positions for CO_2 reduction. The band positions are taken from previous literature.[48−51] The full list of band positions can be found in Figure S7.

appropriate band positions, which enable it to absorb visible light and meanwhile provide enough electromotive force to overcome the large overpotential in CO_2 reduction. (ii) A coherent interface can form between the semiconductor and epitaxial TiO_2, which ensures the stability of thin coating under severe chemical conditions. (iii) The TiO_2 coating has to be within nanometer thickness to allow the tunneling of

photogenerated electrons from the semiconductor to TiO_2 surfaces.

Using the above criteria, we are in a position to examine whether the common photovoltaic semiconductors other than GaP may also act as good photocathodes for CO_2 reduction. To this end, we have screened out the suitable CO_2 reduction candidates from a set of semiconductors involving 21 inorganic semiconductors and seven organic−inorganic hybrid halide perovskites. From their band levels, only three inorganic materials out of 21 candidates have suitable band positions, as shown in Figure 7b, namely AlSb, ZnTe, and AlAs, which can absorb visible light and provide reactive electrons for CO_2 reduction. On the other hand, all seven hybrid halide perovskites solar cells have appropriate band positions for CO_2 reduction.

Next, we examine whether these semiconductors are likely to achieve the coherent interface with TiO_2 coating. Using the modified PTMC method, we find that the low-strain interfaces of $AlSb/TiO_2$, $ZnTe/TiO_2$, and $MAPbI_3/TiO_2$ (MA = $CH_3NH_3^+$) can be obtained and their strains are less than 6%. The ORs for the interfaces are listed in Table S2. This indicates that the low-strain heteromaterial interfaces are not scarce and can, indeed, be searched for from theoretical tools developed here.

5. CONCLUSIONS

By developing a modified PTMC method and combining it with SSW global optimization, we demonstrate that the heteromaterial junctions in general can now be determined from theory rapidly. This has led to the identification of a coherent interface for thin-TiO_2-coated GaP heteromaterial, where the photoelectron is found to tunnel through the nanometer-scale TiO_2 coating layer efficiently. The presence of the coherent interface turns out to be the key structural origin for CO_2 photoreduction. Using the newly developed method, we further predict a number of heteromaterials for visible-light CO_2 photoreduction, including $AlAs/TiO_2$, $AlSb/TiO_2$, $ZnTe/TiO_2$, and $MAPbI_3/TiO_2$, where all three key requirements for visible-light CO_2 photoreduction can be satisfied. Our major results are outlined as follows.

(i) GaP and TiO_2 can form coherent interfaces along three ORs of $(001)_{TiO2}//(100)_{GaP}$, $(101)_{TiO2}//(110)_{GaP}$, and $(112)_{TiO2}//(100)_{GaP}$, corresponding to low interfacial energies of 0.73, 0.76, and 0.83 J/m^2, respectively.

(ii) GaP/TiO_2 heteromaterial has a staggered (type II) gap, where the photoinduced hole prefers to stay on the GaP side while the electron is on the TiO_2 side. The spatial distributions of wave functions for both VBM and CBM are delocalized, and no boundary state exists at the interfaces.

(iii) From the calculated transmission coefficients of carriers (electron or hole) on the coherent TiO_2/GaP interface, we show that hole tunneling occurs only when the TiO_2 coating is thinner than 3 nm and, thus, is sensitive to the TiO_2 thickness; the electron can tunnel through TiO_2 coating without substantial decay. By contrast, the carrier tunneling is much poorer for incoherent interfaces due to the local trapping.

(iv) CO_2 reduction can be promoted significantly only in the presence of tunneled electrons: the highest barrier along the CO_2 reduction pathway is ~1.8 eV on pure TiO_2

and on TiO₂/GaP without tunneling and is only 0.8 eV on TiO₂/GaP when the tunneling occurs.

■ ASSOCIATED CONTENT

Ⓢ Supporting Information

The Supporting Information is available free of charge on the ACS Publications website at DOI: 10.1021/acscatal.9b01645.

Calculation details for the modified PTMC method; discussion about the optimization strategy for GaP/TiO₂ interfaces; details for SSW global structural search; transmission coefficients for electron tunneling through incoherent interface; ORs and lattice parameters for interfaces with strain less than 10%; electronic structures for GaP/TiO₂ heteromaterial by PBE functional; phase diagrams on the surface of GaP/TiO₂ heterojunction; ORs and lattice parameters for interfaces of AlSb/TiO₂, ZnTe/TiO₂, and MAPbI₃/TiO₂ heteromaterials with reasonable strain (<10%); density of states for GaP/TiO₂ heteromaterials; isosurfaces for wave functions of VBM and CBM in GaP/TiO₂ heteromaterials for OR₂ and OR₃; isosurfaces for wave functions of VBM and CBM in GaP/TiO₂ heteromaterials incoherent interface; spatial distribution of spin density for TS1 of CO₂ reduction; band alignment of 21 inorganic semiconductors and seven inorganic–organic hybrid halide perovskites (PDF)

■ AUTHOR INFORMATION

Corresponding Authors
*E-mail: yefeil@fudan.edu.cn.
*E-mail: zpliu@fudan.edu.cn.

ORCID Ⓞ
Ye-Fei Li: 0000-0003-4433-7433
Zhi-Pan Liu: 0000-0002-2906-5217

Notes
The authors declare no competing financial interest.

■ ACKNOWLEDGMENTS

■ REFERENCES

(1) Hansen, H. A.; Varley, J. B.; Peterson, A. A.; Norskov, J. K. Understanding Trends in the Electrocatalytic Activity of Metals and Enzymes for CO₂ Reduction to CO. *J. Phys. Chem. Lett.* 2013, 4, 388−392.

(2) Varley, J. B.; Hansen, H. A.; Ammitzbøll, N. L.; Grabow, L. C.; Peterson, A. A.; Rossmeisl, J.; Nørskov, J. K. Ni-Fe-S Cubanes in CO₂ Reduction Electrocatalysis: A DFT Study. *ACS Catal.* 2013, 3, 2640−2643.

(3) Kumar, B.; Llorente, M.; Froehlich, J.; Dang, T.; Sathrum, A.; Kubiak, C. P. Photochemical and Photoelectrochemical Reduction of CO₂. *Annu. Rev. Phys. Chem.* 2012, 63, 541−569.

(4) Zeng, G. T.; Qiu, J.; Li, Z.; Pavaskar, P.; Cronin, S. B. CO₂ Reduction to Methanol on TiO₂-Passivated GaP Photocatalysts. *ACS Catal.* 2014, 4, 3512−3516.

(5) Chen, Y. W.; Prange, J. D.; Dühnen, S.; Park, Y.; Gunji, M.; Chidsey, C. E. D.; McIntyre, P. C. AtomicLayer-deposited Tunnel Oxide Stabilizes Silicon Photoanodes for Water Oxidation. *Nat. Mater.* 2011, 10, 539.

(6) Scheuermann, A. G.; Prange, J. D.; Gunji, M.; Chidsey, C. E. D.; McIntyre, P. C. Effects of Catalyst Material and Atomic layer Deposited TiO₂Oxide Thickness on the Water Oxidation Performance of Metal-insulator-silicon Anodes. *Energy Environ. Sci.* 2013, 6, 2487−2496.

(7) Qiu, J.; Zeng, G.; Ha, M.-A.; Ge, M.; Lin, Y.; Hettick, M.; Hou, B.; Alexandrova, A. N.; Javey, A.; Cronin, S. B. Artificial Photosynthesis on TiO₂-Passivated InP Nanopillars. *Nano Lett.* 2015, 15, 6177−6181.

(8) Lin, Y.; Kapadia, R.; Yang, J.; Zheng, M.; Chen, K.; Hettick, M.; Yin, X.; Battaglia, C.; Sharp, I. D.; Ager, J. W.; Javey, A. Role of TiO₂ Surface Passivation on Improving the Performance of p-InP Photocathodes. *J. Phys. Chem. C* 2015, 119, 2308−2313.

(9) Bae, D.; Seger, B.; Vesborg, P. C. K.; Hansen, O.; Chorkendorff, I. Strategies for Stable Water Splitting via Protected Photoelectrodes. *Chem. Soc. Rev.* 2017, 46, 1933−1954.

(10) Sun, K.; Shen, S.; Liang, Y.; Burrows, P. E.; Mao, S. S.; Wang, D. Enabling Silicon for Solar-Fuel Production. *Chem. Rev.* 2014, 114, 8662−8719.

(11) Yao, T.; Chen, R.; Li, J.; Han, J.; Qin, W.; Wang, H.; Shi, J.; Fan, F.; Li, C. Manipulating the Interfacial Energetics of n-type Silicon Photoanode for Efficient Water Oxidation. *J. Am. Chem. Soc.* 2016, 138, 13664−13672.

(12) Hu, S.; Shaner, M. R.; Beardslee, J. A.; Lichterman, M.; Brunschwig, B. S.; Lewis, N. S. Amorphous TiO₂Coatings Stabilize Si, GaAs, and GaPPhotoanodes for Efficient Water Oxidation. *Science* 2014, 344, 1005−1009.

(13) Thulin, L.; Guerra, J. Calculations of strain-modified anatase TiO₂ band structures. *Phys. Rev. B: Condens. Matter Mater. Phys.* 2008, 77, 5.

(14) Zhao, X.; Shu, Q.; Nguyen, M. C.; Wang, Y.; Ji, M.; Xiang, H.; Ho, K.-M.; Gong, X.; Wang, C.-Z. Interface Structure Prediction from First-Principles. *J. Phys. Chem. C* 2014, 118, 9524−9530.

(15) Zhang, L.; Jing, D.; She, X.; Liu, H.; Yang, D.; Lu, Y.; Li, J.; Zheng, Z.; Guo, L. Heterojunctions in g-C₃N₄/TiO₂(B) Nanofibres with Exposed (001) Plane and Enhanced Visible-light Photoactivity. *J. Mater. Chem. A* 2014, 2, 2071−2078.

(16) Wayman, C. M. The Phenomenological Theory of Martensite Crystallography: Interrelationships. *Metall. Mater. Trans. A* 1994, 25, 1787−1795.

(17) Bowles, J. S.; Mackenzie, J. K. The Crystallography of Martensite Transformations I. *Acta Metall.* 1954, 2, 129−137.

(18) Mackenzie, J. K.; Bowles, J. S. The Crystallography of Martensite Transformations II. *Acta Metall.* 1954, 2, 138−147.

(19) Zhang, X.-J.; Liu, Z.-P. Variable-Cell Double-Ended Surface Walking Method for Fast Transition State Location of Solid Phase Transitions. *J. Chem. Theory Comput.* 2015, 11, 4885−4894.

(20) Zhang, X.-J.; Shang, C.; Liu, Z.-P. Double-Ended Surface Walking Method for Pathway Building and Transition State Location of Complex Reactions. *J. Chem. Theory Comput.* 2013, 9, 5745−5753.

(21) Shang, C.; Zhang, X. J.; Liu, Z. P. Stochastic Surface Walking Method for Crystal Structure and Phase Transition Pathway Prediction. *Phys. Chem. Chem. Phys.* 2014, 16, 17845−56.

(22) Shang, C.; Liu, Z. P. Stochastic Surface Walking Method for Structure Prediction and Pathway Searching. *J. Chem. Theory Comput.* 2013, 9, 1838−1845.

(23) Li, Y.-F. First Principles Simulations for Morphology and Structural Evolutions of Catalysts in Oxygen Evolution Reaction. *ChemSusChem* 2019, 12, 1846.

(24) Yin, J.; Li, Y.; Lv, F.; Lu, M.; Sun, K.; Wang, W.; Wang, L.; Cheng, F.; Li, Y.; Xi, P.; Guo, S. Oxygen Vacancies Dominated NiS₂/CoS₂ Interface Porous Nanowires for Portable Zn-Air Batteries Driven Water Splitting Devices. *Adv. Mater.* 2017, 29, 1704681.

(25) Guan, S.-H.; Zhang, X.-J.; Liu, Z.-P. Energy Landscape of Zirconia Phase Transitions. *J. Am. Chem. Soc.* 2015, 137, 8010−8013.

(26) Kresse, G.; Furthmüller, J. Efficient Iterative Schemes for ab initio Total-energy Calculations using a Plane-wave Basis Set. *Phys. Rev. B: Condens. Matter Mater. Phys.* **1996**, *54*, 11169.

(27) Soler, J. M.; Artacho, E.; Gale, J. d.; Garcia, A.; Junquera, J.; Ordejón, P.; Sánchez-Portal, D. The SIESTA Method for ab initio Order-N Materials Simulation. *J. Phys.: Condens. Matter* **2002**, *14*, 2745.

(28) Perdew, J. P.; Burke, K.; Ernzerhof, M. Generalized Gradient Approximation Made Simple. *Phys. Rev. Lett.* **1996**, *77*, 3865−3868.

(29) Heyd, J.; Scuseria, G. E.; Ernzerhof, M. Hybrid Functionals Based on a Screened Coulomb Potential. *J. Chem. Phys.* **2003**, *118*, 8207−8215.

(30) Huang, S.-D.; Shang, C.; Kang, P.-L.; Zhang, X.-J.; Liu, Z.-P. LASP: Fast Global Potential Energy Surface Exploration. *WIRes. Comput. Mol. Sci.* **2019**, No. e1415.

(31) Levi, A. F. J. *Applied Quantum Mechanics*; Cambridge University Press, 2006.

(32) Yao, X.; Chen, L.; Liu, M.; Feng, D.; Wang, C.; Lu, F.; Wang, W.; Wang, X.; Cheng, Y.; Liu, H.; Chen, H.; Wang, W. Rational Design of Si/TiO$_2$Heterojunction Photocatalysts: Transfer Matrix Method. *Appl. Catal., B* **2018**, *221*, 70−76.

(33) Bastos, C. M. O.; Sabino, F. P.; Sipahi, G. M.; Da Silva, J. L. F. A Comprehensive Study of g-Factors, Elastic, Structural and Electronic Properties of III-V Semiconductors using Hybrid-density Functional Theory. *J. Appl. Phys.* **2018**, *123*, 065702.

(34) Zhang, J.; Zhou, P.; Liu, J.; Yu, J. New Understanding of the Difference of Photocatalytic Activity among Anatase, Rutile and Brookite TiO$_2$. *Phys. Chem. Chem. Phys.* **2014**, *16*, 20382−20386.

(35) Chua, A. L. S.; Benedek, N. A.; Chen, L.; Finnis, M. W.; Sutton, A. P. A Genetic Algorithm for Predicting the Structures of Interfaces in Multicomponent Systems. *Nat. Mater.* **2010**, *9*, 418.

(36) Li, Y.-F.; Liu, Z.-P.; Liu, L.; Gao, W. Mechanism and Activity of Photocatalytic Oxygen Evolution on Titania Anatase in Aqueous Surroundings. *J. Am. Chem. Soc.* **2010**, *132*, 13008−13015.

(37) Wang, D.; Sheng, T.; Chen, J.; Wang, H.-F.; Hu, P. Identifying the Key Obstacle in Photocatalytic Oxygen Evolution on Rutile TiO$_2$. *Nature Catal.* **2018**, *1*, 291−299.

(38) Dhakshinamoorthy, A.; Navalon, S.; Corma, A.; Garcia, H. Photocatalytic CO$_2$Reduction by TiO$_2$ and Related Titanium Containing Solids. *Energy Environ. Sci.* **2012**, *5*, 9217−9233.

(39) Street, R. A.; Krakaris, A.; Cowan, S. R. Recombination through Different Types of Localized States in Organic Solar Cells. *Adv. Funct. Mater.* **2012**, *22*, 4608−4619.

(40) Williams, O. M.; Shi, J. W.; Rose, M. J. Photoelectrochemical Study of p-GaP(100)ZnOAuNPDevices: Strategies for Enhanced Electron Transfer and Aqueous Catalysis. *Chem. Commun.* **2016**, *52*, 9145−9148.

(41) Ji, Y.; Luo, Y. Theoretical Study on the Mechanism of Photoreduction of CO$_2$ to CH$_4$ on the Anatase TiO$_2$(101) Surface. *ACS Catal.* **2016**, *6*, 2018−2025.

(42) Ji, Y.; Luo, Y. New Mechanism for Photocatalytic Reduction of CO$_2$ on the Anatase TiO$_2$(101) Surface: The Essential Role of Oxygen Vacancy. *J. Am. Chem. Soc.* **2016**, *138*, 15896−15902.

(43) Anslyn, E. V.; Dougherty, D. A. *Modern Physical Organic Chemistry*; University Science Books, 2006.

(44) Marcì, G.; García-López, E. I.; Palmisano, L. Photocatalytic CO$_2$Reduction in Gas-solid Regime in the Presence of H$_2$O by using GaP/TiO$_2$Composite as Photocatalyst under Simulated Solar Light. *Catal. Commun.* **2014**, *53*, 38−41.

(45) Fang, Y.-H.; Liu, Z.-P. Mechanism and Tafel Lines of Electro-Oxidation of Water to Oxygen on RuO$_2$(110). *J. Am. Chem. Soc.* **2010**, *132*, 18214−18222.

(46) Marcus, R. A. On the Theory of Chemiluminescent Electron-Transfer Reactions. *J. Chem. Phys.* **1965**, *43*, 2654−2657.

(47) Marcus, R. A. On the Theory of Electron-Transfer Reactions. VI. Unified Treatment for Homogeneous and Electrode Reactions. *J. Chem. Phys.* **1965**, *43*, 679−701.

(48) Grüneis, A.; Kresse, G.; Hinuma, Y.; Oba, F. Ionization Potentials of Solids: The Importance of Vertex Corrections. *Phys. Rev. Lett.* **2014**, *112*, 5.

(49) Hinuma, Y.; Gruneis, A.; Kresse, G.; Oba, F. Band alignment of Semiconductors from Density-functional Theory and Many-body Perturbation Theory. *Phys. Rev. B: Condens. Matter Mater. Phys.* **2014**, *90*, 16.

(50) Chueh, C. C.; Li, C. Z.; Jen, A. K. Y. Recent Progress and Perspective in Solution-processed Interfacial Materials for Efficient and Stable Polymer and Organometal Perovskite Solar Cells. *Energy Environ. Sci.* **2015**, *8*, 1160−1189.

(51) Zardetto, V.; Williams, B. L.; Perrotta, A.; Di Giacomo, F.; Verheijen, M. A.; Andriessen, R.; Kessels, W. M. M.; Creatore, M. Atomic Layer Deposition for Perovskite Solar Cells: Research status, Opportunities and Challenges. *Sustain. Energy Fuels* **2017**, *1*, 30−55.